Supporting information for: Modeling interfacial electron transfer in the double layer: the interplay between electrode coupling and electrostatic driving

Aditya M. Limaye[†] and Adam P. Willard[*,‡]

†*Department of Chemical Engineering, MIT, Cambridge, MA*

‡*Department of Chemistry, MIT, Cambridge, MA*

E-mail: awillard@mit.edu

Non-Dimensionalization Procedure

Conservation of probability mass yields the set of partial differential equations

$$\frac{\partial P_i}{\partial t} = \hat{\mathcal{L}}_i P_i + \sum_{j \neq i} \left[\zeta_{j \to i} P_j - \zeta_{i \to j} P_i \right]. \tag{1}$$

Expanding the shorthand for the Smoluchowski propagator,

$$\frac{\partial P_i}{\partial t} = \mathcal{D} \nabla \cdot \left[e^{-\beta F_i} \nabla \left(e^{\beta F_i} P_i \right) \right] + \sum_{j \neq i} \left[\zeta_{j \to i} P_j - \zeta_{i \to j} P_i \right]. \tag{2}$$

Non-dimensionalizing the gradient operators $\tilde{\nabla} \equiv L \cdot \nabla$,

$$\frac{\partial P_i}{\partial t} = \frac{\mathcal{D}}{L^2} \tilde{\nabla} \cdot \left[e^{-\beta F_i} \tilde{\nabla} \left(e^{\beta F_i} P_i \right) \right] + \sum_{j \neq i} \left[\zeta_{j \to i} P_j - \zeta_{i \to j} P_i \right]. \tag{3}$$

As explained in the main text, the diffusive timescale $\tau \equiv \mathcal{D}/L^2$, implying

$$\tau \frac{\partial P_i}{\partial t} = \tilde{\nabla} \cdot \left[e^{-\beta F_i} \tilde{\nabla} \left(e^{\beta F_i} P_i \right) \right] + \sum_{j \neq i} \left[\tau \cdot \zeta_{j \to i} P_j - \tau \cdot \zeta_{i \to j} P_i \right]. \tag{4}$$

Introducing the non-dimensional time and sink/source rates ($\tilde{t} \equiv t/\tau$ and $\tilde{\zeta_{ij}} \equiv \tau \cdot \zeta_{ij}$) yields the final non-dimensionalized equations

$$\frac{\partial P_i}{\partial \tilde{t}} = \tilde{\nabla} \cdot \left[e^{-\beta F_i} \tilde{\nabla} \left(e^{\beta F_i} P_i \right) \right] + \sum_{j \neq i} \left[\tilde{\zeta}_{j \to i} P_j - \tilde{\zeta}_{i \to j} P_i \right]. \tag{5}$$

Computational Details

Similarity Transformation

The Smoluchowski diffusion operator from the main text reads

$$\hat{\mathcal{L}}_i P_i \equiv \mathcal{D}\nabla \cdot \left[e^{-\beta F_i} \nabla \left(e^{\beta F_i} P_i \right) \right]. \tag{6}$$

As written, this operator is not self-adjoint. This makes numerical solution more difficult, and makes a diagonalization procedure unstable.[S1] A standard similarity transformation[S2] can be employed to write $\hat{\mathcal{L}}_i$ in a self-adjoint form $\hat{\mathcal{L}}_i^H$, formally written as

$$\hat{\mathcal{L}}_i = \exp\left(-\beta F_i/2\right) \hat{\mathcal{L}}_i^H \exp\left(\beta F_i/2\right) \tag{7}$$

Recasting the full population dynamics equations in terms of $\hat{\mathcal{L}}_i^H$ creates some changes to the sink and source terms which render the entire propagator self-adjoint, the details of this transformation have been worked out by Ouyang and Subotnik.[S1] Since the self-adjoint form of the operator is the one we actually use when carrying out numerical calculations, we report a discretization scheme for $\hat{\mathcal{L}}_i^H$, rather than the original propagator.

Interior Point Discretization

We choose a finite-volume discretization of the SME because it explicitly conserves mass to numerical precision and also naturally incorporates no-flux boundary conditions, which are employed at most boundaries in this model. Fig. S1 shows a schematic of one of the node points hosting a finite volume. Our charge is to discretize the self-adjoint version of the Smoluchowski propagator, written as

$$\hat{\mathcal{L}}^H = e^{\beta F/2} \frac{\partial}{\partial x_i} e^{-\beta F} \frac{\partial}{\partial x_i} e^{\beta F/2}, \tag{8}$$

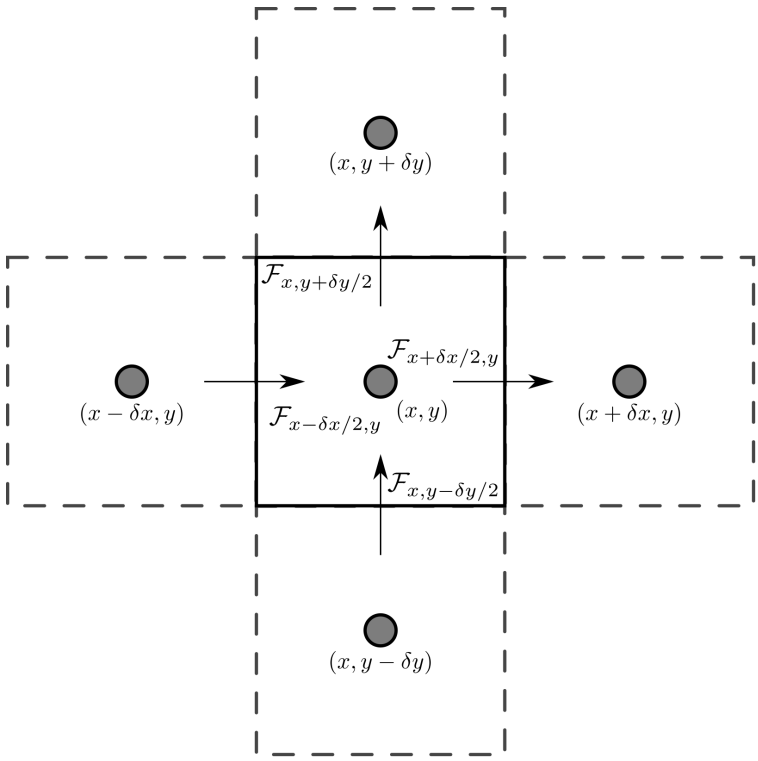

Figure S1: Schematic of the finite-volume discretization used for numerical solution of the Smoluchowski master equation.

where x_i is a generalized coordinate (here, refers to either x or z), and Einstein summation is implied. Inspection reveals that the operator in Eq. (8) is a (weighted) divergence of flux terms.

Using a two-point forward difference stencil, the appropriately-weighted fluxes piercing

the boundary surfaces in Fig. S1 of an interior point can be expressed as

$$\mathcal{F}_{x-\delta x/2,y} = \exp\left[-\beta F(x-\delta x/2,y)\right]\left[\frac{\exp\left[\beta F(x,y)/2\right]P(x,y) - \exp\left[\beta F(x-\delta x,y)/2\right]P(x-\delta x,y)}{\delta x}\right] \tag{9}$$

$$\mathcal{F}_{x+\delta x/2,y} = \exp\left[-\beta F(x+\delta x/2,y)\right]\left[\frac{\exp\left[\beta F(x+\delta x,y)/2\right]P(x+\delta x,y) - \exp\left[\beta F(x,y)/2\right]P(x,y)}{\delta x}\right] \tag{10}$$

$$\mathcal{F}_{x,y-\delta y/2} = \exp\left[-\beta F(x,y-\delta y/2)\right]\left[\frac{\exp\left[\beta F(x,y)/2\right]P(x,y) - \exp\left[\beta F(x,y-\delta y)/2\right]P(x,y-\delta y)}{\delta y}\right] \tag{11}$$

$$\mathcal{F}_{x,y+\delta y/2} = \exp\left[-\beta F(x,y+\delta y/2)\right]\left[\frac{\exp\left[\beta F(x,y+\delta y)/2\right]P(x,y+\delta y) - \exp\left[\beta F(x,y)/2\right]P(x,y)}{\delta y}\right] \tag{12}$$

The diffusion operator can now be assembled by weighting the fluxes by their appropriate Boltzmann weight from Eq. (6) and making a first order central finite difference approximation for the divergence. The diffusion operator at a node point centered at (x, y) can be expressed as

$$\begin{aligned}\mathcal{L}^H(x,y) = &\frac{\exp\left[\beta F(x+\delta x/2,y)/2\right]\mathcal{F}_{x+\delta x/2,y} - \exp\left[\beta F(x-\delta x/2,y)/2\right]\mathcal{F}_{x-\delta x/2,y}}{\delta x} \\ &+ \frac{\exp\left[\beta F(x,y+\delta y/2)/2\right]\mathcal{F}_{x,y+\delta y/2} - \exp\left[\beta F(x,y-\delta y/2)/2\right]\mathcal{F}_{x,y-\delta y/2}}{\delta y}\end{aligned} \tag{13}$$

Note that Eq. (13) requires evaluating the free energy on the dual grid of the grid defining the node points; this is not difficult if the free energy can be expressed as an analytical function in closed form, as in this work.

Boundary Point Discretization

At boundary points, we have to take additional care to implement the appropriate boundary condition. No-flux (Neumann) conditions are simple to incorporate into the discretization scheme, we simply need to set the corresponding boundary flux term in Eq. (13) to zero. This results in a closed set of equations; the values of the probability field at the interior points are the only dependent variables involved.

Concentration (Dirichlet) boundary conditions are slightly more difficult to implement. The two-point central difference flux stencils in Eqns. (9)–(12) must be changed to two-point *forward* difference stencils that involve the specified boundary probability. For the flux $\mathcal{F}_{x,y+\delta y/2}$ out of a top boundary with a specified boundary probability,

$$\mathcal{F}_{x,y+\delta y/2} = \exp\left[-\beta F(x, y+\delta y/2)\right] \left[\frac{\exp\left[\beta F(x, y+\delta y/2)/2\right] P_{\text{bdy.}}(x) - \exp\left[\beta F(x,y)/2\right] P(x,y)}{(\delta y/2)}\right], \tag{14}$$

where $P_{\text{bdy.}}(x)$ is the boundary probability. Note that the first term in the bracketed expression is a constant, while the second term involves a dependent field variable. The first term comprises an inhomogeneity in the propagator, and leads to the existence of a non-trivial steady state solution.

Steady-State Solution

The discretization scheme described in the previous two sections approximates the unbounded Smoluchowski diffusion operator in Eq. (6) by a bounded finite difference operator. The hopping terms can be included straightforwardly[S1] into the bounded difference operator, reducing the population dynamics partial differential equation to the matrix equation

$$\frac{\mathrm{d}\mathbf{p}}{\mathrm{d}t} = \mathbf{L}\mathbf{p} + \mathbf{c}, \tag{15}$$

where $\mathbf{L}$ is the matrix encoding the bounded propagator, $\mathbf{p}$ is the probability distribution evaluated at the finite difference nodes, and $\mathbf{c}$ is a constant inhomogeneity vector arising from the Dirichlet boundary conditions. The solution of the system

$$\mathbf{L}\mathbf{p} = -\mathbf{c} \tag{16}$$

comprises a steady-state of the SME model. In practice, the $\mathbf{L}$ operator is very sparse with a predictable structure (block-diagonal with appropriate bandwidth), and so sparse matrix algorithms can be used to efficiently solve the system in Eq. (16).

Computing Current

Comparing results from the SME model to experimental current-voltage data requires a working definition for net ET current towards a single species. If we let $P_i(x, z)$ denote the steady-state probability distributions of the species given the appropriate boundary conditions, an intuitive definition of the net ET current towards species k is:

$$\mathcal{J}_k \equiv \int \mathrm{d}x\mathrm{d}z \sum_{j \neq k} [P_j \cdot \zeta_{j \to k} - P_k \cdot \zeta_{k \to j}] \tag{17}$$

Alternatively, we can compute the current by integrating the net probability flux out of the $z = 1$ boundary for species k. While appropriate as a definition for the current, this is more numerically ill-conditioned since it involves a finite difference expression at a point where the potential profile has a corner. This ill-conditioning becomes worse at higher values of the applied potential. For all current-voltage curves measured here, we use the definition in Eq. (17), which is numerically robust over a wide range of applied potentials.

Transfer Coefficients

Traditional Marcus Theory

Marcus theory provides a prediction for the dependence of the transfer coefficient on the applied potential. I will reproduce the derivation of this dependence here using the parameters defined in the two-surface model; the end result is identical to the textbook result[S3] with appropriate redefinition of variables. Take two Marcus free energies defined on a single coordinate x:

$$f_1(x) = \frac{k_{\text{reorg}}}{2} \cdot (x-1)^2 \tag{18}$$

$$f_2(x) = \frac{k_{\text{reorg}}}{2} \cdot x^2 + \Delta E_{\text{int}} + eV, \tag{19}$$

where V is the applied potential. The two curves intersect at:

$$x^* = \frac{1}{2} - \frac{\Delta E_{\text{int}} + eV}{k_{\text{reorg}}} \tag{20}$$

The free energy at this point referenced to the minimum of f_1 is exactly the activation energy E_a, and is given by:

$$E_a = \frac{k_{\text{reorg}}}{2} \left[\frac{1}{2} + \frac{\Delta E_{\text{int}} + eV}{k_{\text{reorg}}}\right]^2 \tag{21}$$

Therefore,

$$\alpha_{\text{Marcus}} = -\frac{\partial E_a}{\partial (eV)} = \left[\frac{1}{2} + \frac{\Delta E_{\text{int}} + eV}{k_{\text{reorg}}}\right]. \tag{22}$$

Eq. (22) is identical to the one produced in the main text.

Model for Transfer Coefficient Attenuation

The model for transfer coefficient attenuation relies on the calculation of an activation energy profile over the approach coordinate. We can derive this in a similar manner to the traditional

Marcus derivation. The two Marcus free energies are now defined over the product space (x, z):

$$f_1(x, z) = \frac{k_{\text{reorg}}}{2} \cdot (x-1)^2 \tag{23}$$

$$f_2(x, z) = \frac{k_{\text{reorg}}}{2} \cdot x^2 + \Delta E_{\text{int}} + eVz, \tag{24}$$

The two curves intersect at:

$$x^* = \frac{1}{2} - \frac{\Delta E_{\text{int}} + eVz}{k_{\text{reorg}}} \tag{25}$$

The activation energy profile is straightforward to calculate from here:

$$E_a(z) = \frac{k_{\text{reorg}}}{2} \left[\frac{1}{2} + \frac{\Delta E_{\text{int}} + eVz}{k_{\text{reorg}}}\right]^2 \tag{26}$$

Applying the Leibniz rule requires computing

$$\frac{\mathrm{d}E_a}{\mathrm{d}(eV)} = z \left[\frac{1}{2} + \frac{\Delta E_{\text{int}} + Vz}{k_{\text{reorg}}}\right] \tag{27}$$

The final transfer coefficient expression from the main text is

$$\alpha = -\int \mathrm{d}z \; \tilde{\tilde{\Delta}}(z) \cdot \left[\frac{\mathrm{d}E_a}{\mathrm{d}(eV)}\right] \;, \tag{28}$$

Fig. S2 depicts a graphical representation of the integral in Eq. (28), using the same parameters discussed in the main text, for $V = -0.20$ V (zero overpotential). Current distributions that are highly localized near the electrode surface ($z = 0$) overlap with the initial, increasing branch of this function, and lead to low transfer coefficients. When the ET event is entirely localized to the EDL boundary, implying that $\tilde{\tilde{\Delta}}(z) = \delta[z-1]$, then the integration "sifts out" the value of Eq. (27) at $z = 1$. At zero overpotential, this value is exactly 1/2, implying that we recover the Marcus result from Eq. (22) in the appropriate limit.

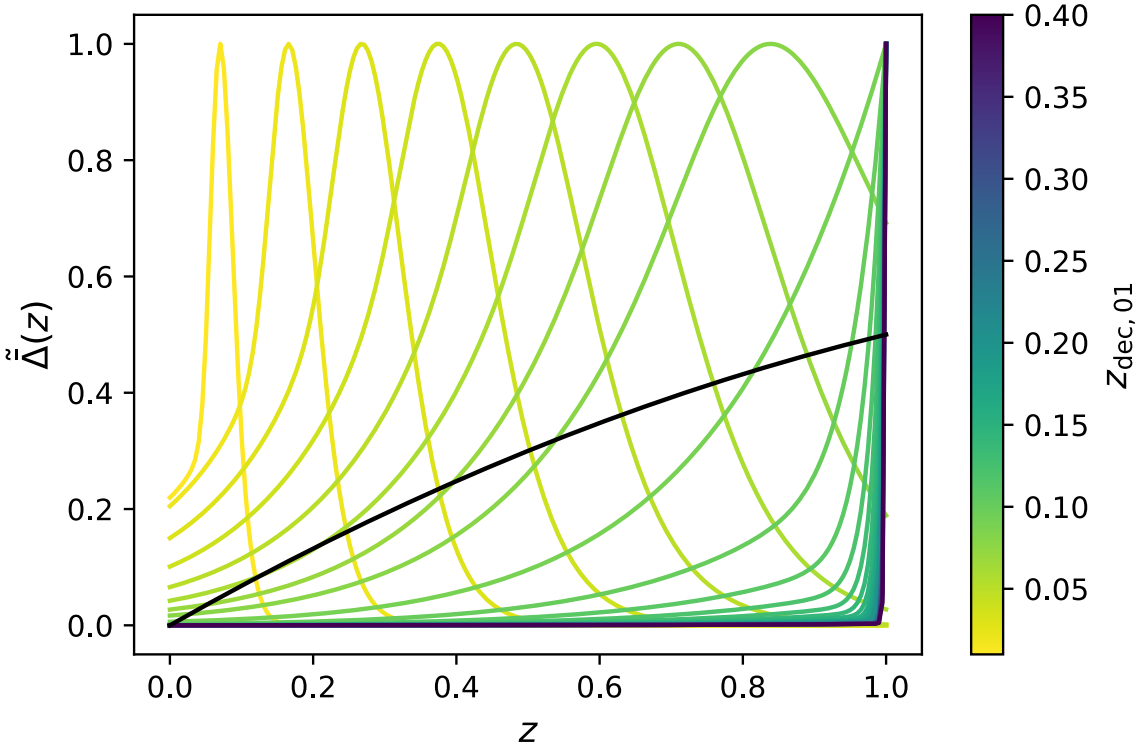

Figure S2: Traces of the normalized marginal current $\tilde{\tilde{\Delta}}(z)$ for values of $z_{\mathrm{dec,01}} \in [0.01, 0.40]$, as well as a plot of the integration weight function in Eq. (27).

Potential Dependence of the Net Current Profile

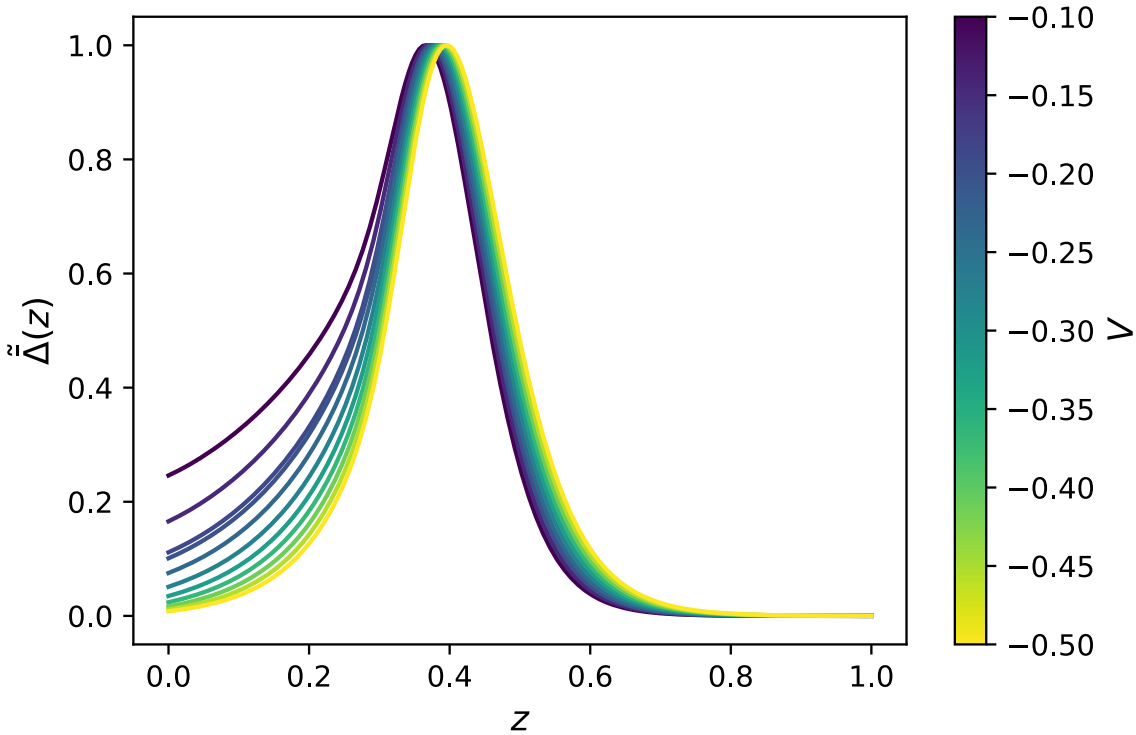

Figure S3: Normalized net current marginal profiles for a range of values of the applied voltage, using the same parameters as the main text. The shape of the profile is a weak function of the applied voltage.

The derivation of the transfer coefficient model in the main text employed an assumption that the normalized net current marginal $\tilde{\tilde{\Delta}}(z)$ was roughly independent of the applied voltage. Figure S3 provides numerical confirmation that the net current marginal profile is only a weak function of voltage over the voltage range studied. Note that this is only an appropriate assumption when the reactant species does not carry a charge. For a charged reactant, the ET localization behavior is a strong function of potential, as discussed in the main text.

Additional Intuition

The main text makes reference to a "pinning" effect that attenuates the transfer coefficient as a consequence of ET localization near the electrode surface. Fig. S4 provides some schematic intuition for this phenomenon. Since the driving force is constrained to be exactly zero at the electrode surface, modulating the voltage yields less "bang for the buck" activation energy-wise when the ET event is constrained to occur near the electrode.

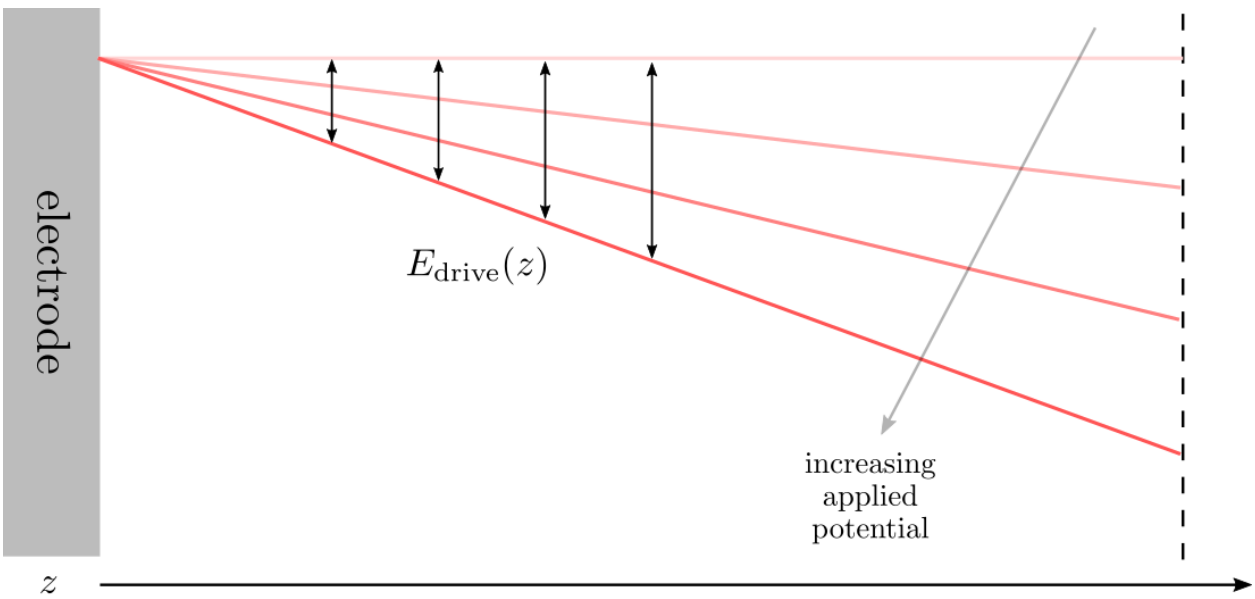

Figure S4: Schematic picture of the distance-dependent potential driving force in the SME model with linear potential decay. As ET occurs closer to the electrode, modulating the external potential has a smaller effect on the potential driving force felt by the redox-active species.

Results for Higher Reorganization Energy

A replication of Figure 3 from the main text, but with $k = 2.00$ eV. As expected, for higher reorganization energies, the current-voltage curves are linear over a broader voltage range, and the transfer coefficient prediction from Eq. (28) is more quantitatively correct.

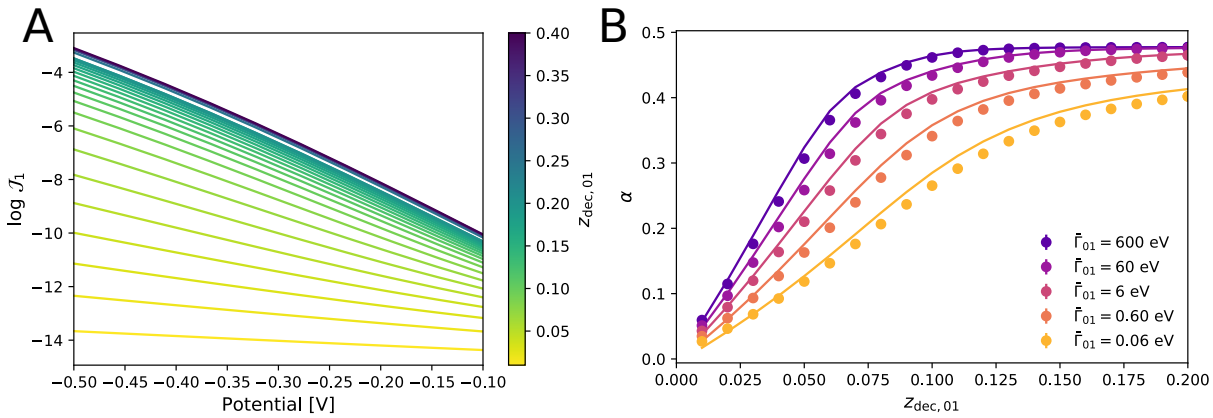

Figure S5: Current-voltage curves and transfer coefficient predictions from the two-surface model, for $k_{\mathrm{reorg}} = 2.00$ eV. (A) Several current-voltage curves measured for different values of the coupling localization parameter $z_{\mathrm{dec},01}$, with $\bar{\Gamma}_{01} = 6$ eV. (B) Transfer coefficients determined by linear fitting for a number of different coupling strengths are shown as colored dots. The solid lines are predictions from the simple model/approximation developed in Eq. (28).

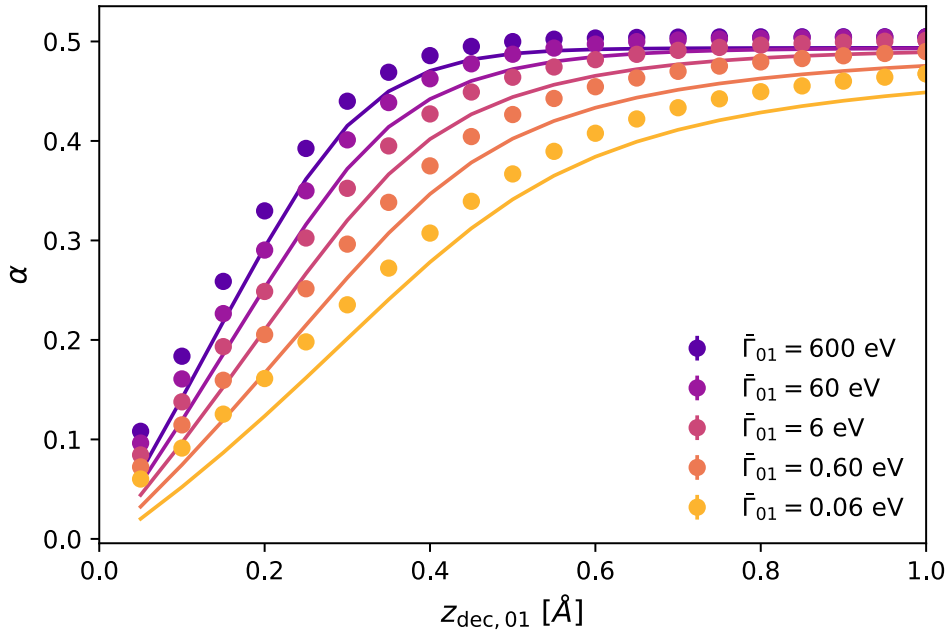

Figure S6: Transfer coefficients determined from linear fitting of current-voltage behavior versus $z_{\mathrm{dec},01}$, presented here on a dimensional scale, assuming $L = 5$ Å.

Dimensionalized Results for Transfer Coefficient Attenuation

A replication of Figure 3B from the main text, but this time with the parameter $z_{\text{dec},01}$ presented on a dimensional scale, taking $L = 5$ $\mathring{A}$, characteristic for an aqueous electrolyte with a 1M concentration of monovalent salt. We hope this helps contextualize the results presented in the main text in terms of length scales familiar to electrochemical literature.

Results for Exponential Potential Decay Profile

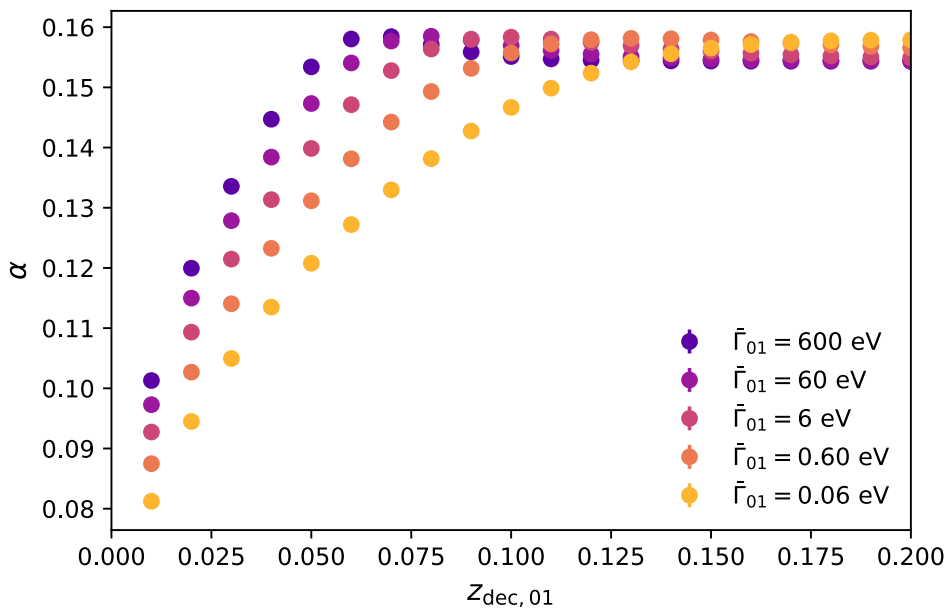

Figure S7: Transfer coefficients determined from linear fitting of current-voltage behavior versus $z_{\text{dec},01}$ from a model using the Gouy-Chapman potential decay profile in Eq. (29).

A replication of Figure 3B from the main text, but with an augmented potential profile,

$$\phi(z) = V \exp\left[-\frac{z}{\nu}\right], \tag{29}$$

representing the Gouy-Chapman solution to potential decay in an electrolyte with mobile charges at a plane interface held at constant potential. In these simulations, we set $\nu = 0.285L$. Note that the solid lines from the main-text figure are derived from an analytical approximation that only holds for the linear decay profile presented in the main text, so the

solid lines are omitted from this figure.

References

(S1) Ouyang, W.; Subotnik, J. E. The dynamics of charge transfer with and without a barrier: A very simplified model of cyclic voltammetry. *The Journal of chemical physics* **2017**, *146*, 174103.

(S2) Risken, H.; Frank, T. The Fokker-Planck Equation: Methods of Solutions and Applications (Springer Series in Synergetics). *Springer* **1996**,

(S3) Bard, A. J.; Faulkner, L. R.; Leddy, J.; Zoski, C. G. *Electrochemical methods: fundamentals and applications*; Wiley New York, 1980; Vol. 2.